ACS SENSORS

pubs.acs.org/acssensors

Article

miniSPIM—A Miniaturized Light-Sheet Microscope

Per Niklas Hedde*

Cite This: *ACS Sens.* 2021, 6, 2654–2663

Read Online

ACCESS | Metrics & More | Article Recommendations | Supporting Information

ABSTRACT: The miniSPIM is a miniaturized light-sheet microscope that enables imaging with optical sectioning on mobile camera devices such as smartphones and single-board computers. Applications of the miniSPIM include biosensing, field research, and education where maximum portability and robustness, low power consumption, and low cost are key. Here, it is shown how all of the components of a simple light-sheet microscope can be integrated within a footprint smaller than the average smartphone. Example applications include the quantification of the motion of microparticles and bacteria in fluids, the characterization of solvent polarity based on spectral shifts of the lipid probe Nile Red, and three-dimensional (3D) and time-lapse autofluorescence imaging of a live zebrafish embryo.

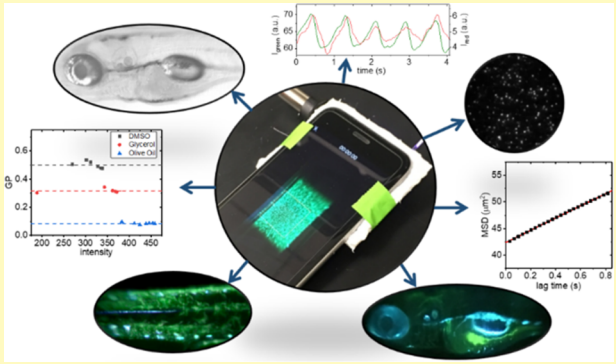

KEYWORDS: *selective plane illumination microscopy, light-sheet microscopy, three-dimensional imaging, optical sectioning, bacteria detection, particle detection, fluorescence fluctuation spectroscopy, image correlation spectroscopy*

In recent years, mobile electronic devices such as smartphones, tablets, and wearables have become more and more sophisticated. They feature a variety of sensors such as high-resolution cameras, are equipped with the latest communication technology including wireless data transfer, and their computational power exceeds previously available desktop computers. Due to these properties, portable devices have great potential in biomedical and biosensing applications allowing for fast, inexpensive on-site diagnosis using imaging-based methods. One of the most suitable techniques for fast imaging with optical sectioning in three-dimensional environments with a camera is selective or single-plane illumination (SPIM), where sample illumination is confined to the plane of observation with a thin sheet of light. The miniSPIM presented here describes a miniaturized, low-cost light-sheet microscope based on a mobile device equipped with a camera that can be used for remote biosensing applications, field research, and for teaching the fundamentals of optics and biophotonics.

Despite being a well-known principle for over a century, the use of light-sheet microscopy[1] only recently has found widespread application in research due to advances in detector technology and data processing.[2,3] Typically, the light sheet is generated by injecting the light at a 90° angle with respect to the detection axis with cylindrical optics. Instead of using a cylinder lens, a virtual sheet can be generated by rapidly scanning the excitation beam across the observation plane. In either case, by restricting the illumination to a plane, light-sheet microscopy is one of the most powerful approaches for fast imaging with optical sectioning.[4] Different instrument designs allow light-sheet microscopy to cover a broad range of object sizes ranging from entire mouse brains (>10 mm) down to structures inside cell nuclei (<1 μm). Popular applications include developmental studies in embryos of small organisms such as fruit flies,[5] worms,[6] and zebrafish,[2] imaging of cleared brain tissue,[7] nondestructive pathology of clinical specimens,[8] screening of well plates,[9] single-cell imaging,[10] and single-particle tracking and single-molecule dynamics.[11,12] Widespread application of light-sheet microscopy has been further encouraged through the recent development of several open-source light-sheet platforms including standalone platforms,[13−16] adapters to add light-sheet illumination to existing epifluorescence microscopes,[17,18] and platforms tailored for specific applications such as fluidics[19,20] or cleared tissues.[21] However, despite their streamlined design, these instruments are intended for stationary use and are thus relatively large and expensive. On the other hand, various adapters for microscopy using portable devices such as smartphones have been developed. For mobile camera devices, different illumination strategies have been reported including on-axis epi-illumination,[22−24] off-axis inclined illumination,[25] butt-coupling,[26] using microlenses,[27] and total internal reflection.[28] To avoid out-of-focus background with these illumination schemes, the sample can either be compressed to a thickness of <10 μm by mounting it between two glass slides[29] or

Received: March 24, 2021
Accepted: June 18, 2021
Published: July 1, 2021

https://doi.org/10.1021/acssensors.1c00607
ACS Sens. 2021, 6, 2654–2663

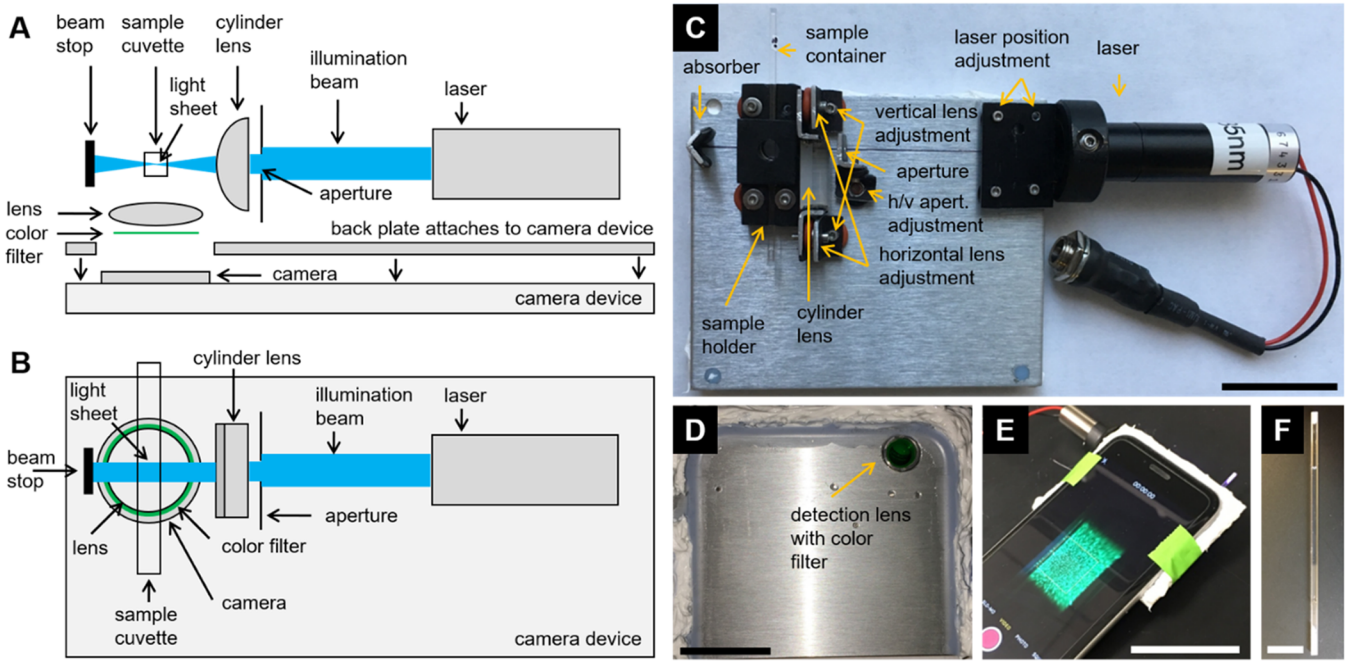

Figure 1. miniSPIM schematic and photographs. (A) Side view and (B) top view of the miniSPIM components. The output of a laser diode (635 or 445 nm) was cleaned with a circular aperture (1.6 mm diameter) before focusing into a sheet of light at the sample plane with a cylindrical lens (f = 10 mm); a beam stop ensured that no laser light left the device. Fluorescence was collected perpendicular to the excitation axis with an aspheric lens (f = 4.6 mm) and separated from scattered excitation light with an emission filter (Kodak Wratten No 55 or No 12) sandwiched between the detection lens and the mobile device camera. A square glass cuvette (1 mm inner diameter, 1.4 mm outer diameter, 50 mm length) was used to contain the sample. (C) Top-view photograph of the assembled miniSPIM system. Scale bar: 25 mm. (D) Bottom-view photograph of the miniSPIM showing the lens and filter that interface with the mobile device camera. Scale bar: 25 mm. (E) Silicon mold was used to adapt the miniSPIM to the external dimensions of a mobile phone. Scale bar: 50 mm. (F) Photograph of the square sample capillary used to contain the sample. Scale bar: 5 mm.

physical properties of the sample such as plasmonic enhancement due to the presence of a metal surface[25] or total internal reflection due to the presence of a refractive index change can be exploited.[28]

Instead, in this work, plane illumination was used to combine the advantages of light-sheet microscopy with the portability and low cost of mobile camera devices. The design presented here consists of an adapter plate with a compact battery-powered laser diode (e.g., laser pointer) and optics to generate a sheet of light inside a small (1.4 mm × 1.4 mm × 50 mm) inexpensive ($1 each), disposable square cuvette. Integrated into this adapter plate is a lens that magnifies and relays the image of the illuminated plane to the camera of a mobile device such as a smartphone. This design is extremely compact (size of an average smartphone), portable (battery operated), robust (no realignment when changing samples), inexpensive (<$200 excluding mobile camera device), and highly flexible as sample cuvettes can be changed within seconds. With a color camera (RGB), three channels can be imaged simultaneously and the sample cuvette can accommodate a wide range of samples including solutions of particles and small organisms such as bacteria as well as larger objects such as (live) zebrafish embryos. In a first biosensing application, fast video-rate acquisition of the miniSPIM was used to measure the mean square displacement (MSD) of microparticles and bacteria in solution. In a second biosensing application, the polarity of several solvents was quantified based on spectral shifts of the fluorescent lipid probe Nile Red (NR) by means of general polarization (GP) analysis of the color sensor data. Finally, as an example of field research, multichannel autofluorescence imaging of a live zebrafish embryo was demonstrated including time-lapse imaging and three-dimensional (3D) data acquisition.

RESULTS

Optical Component Arrangement for Light-Sheet Microscopy with a Mobile Device. A schematic of the miniSPIM system is depicted in Figure 1A,B. All components were mounted on a thin, rigid surface that acted as a back plate to attach to the mobile camera device used for imaging. The collimated beam from a battery-operated laser diode (445 or 635 nm) was directed onto a circular aperture of 1.6 mm diameter to obtain a uniform beam. A cylinder lens of 10 mm focal length and external dimensions of 9 mm × 14 mm was used to focus the excitation beam into sheets of 3.0 μm and 4.3 μm thickness (Gaussian full width at half-maximum—FWHM) and Rayleigh lengths of 89 and 126 μm for 445 and 635 nm light, respectively. The position of the cylinder lens was adjusted to focus the excitation light at the focal plane of the detection lens, see the Methods section for a description of the alignment procedure. Emission light was collected perpendicular to the illumination axis with an aspheric lens of short focal length (4.6 mm focal length, 4.8 mm clear aperture, 9.2 mm outer diameter, NA 0.5) to relay and magnify the field of view of the mobile device camera. For fluorescence detection, a thin Kodak Wratten No 55 band pass or No 12 long-pass gelatin filter was sandwiched between the detection lens and the camera lens to reject scattered excitation light.

The back plate of the prototype consisted of an aluminum sheet of 1.6 mm thickness. All components were mounted on this plate with 0−80 screws; a photograph of the finished assembly can be seen in Figure 1C. To allow for fine alignment,

https://doi.org/10.1021/acssensors.1c00607
ACS Sens. 2021, 6, 2654−2663

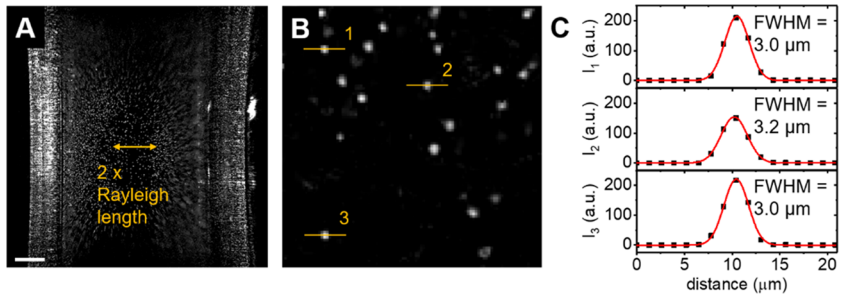

Figure 2. Characterization of the miniSPIM prototype. (A) Scattered light image of a sample cuvette filled with a solution of 1 μm diameter polystyrene particles. Scale bar: 200 μm. Maximum optical sectioning was provided within a distance of 300 μm, corresponding to ~2× the calculated Rayleigh length (indicated by arrow). Spherical aberration distorted the image at the field of view periphery, which was expected due to the simplicity of the detection optics compared to fully corrected high-end microscopy objective lenses. (B) Zoomed-in view of a region within the aberration-free zone; the cross sections of three beads were measured. (C) Cross sections and Gaussian fits of the three particles marked in panel (B); the average full width at half-maximum (FWHM) was 3.1 μm.

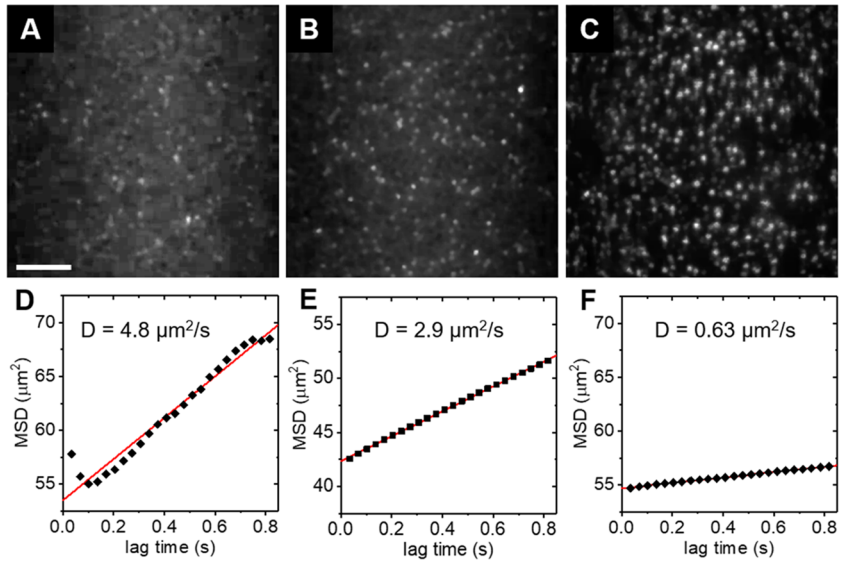

Figure 3. Images and diffusion kinetics of fluorescent beads. (A–C) Example images of aqueous solutions of yellow-green fluorescent beads of 100, 200, and 500 nm diameters. Scale bar: 100 μm. (D–F) Particle mean square displacement (MSD) as a function of lag time obtained by image correlation analysis of 512 frames each recorded at 29.9 fps. The diffusion coefficients obtained by linear regression (red solid lines) were 4.8 $\mu m^2\ s^{-1}$ (100 nm beads), 2.9 $\mu m^2\ s^{-1}$ (200 nm beads), and 0.63 $\mu m^2\ s^{-1}$ (500 nm beads).

individual components were suspended on 1.6 mm thick rubber O-rings. Tightening of the screws compressed the rubber resulting in a translation range along the screw axis of ~0.8 mm. On the front, silicon sealant was used to create a mold matching the dimensions to accommodate a mobile phone camera (see Figure 1D). A photograph of the miniSPIM prototype attached to a smartphone is shown in Figure 1E. This mold could be replaced with an adjustable 3D printable holder that could be adopted to different smartphone models or other portable camera devices. The sample holder featured a square, 1.5 mm wide channel to accommodate a glass cuvette. An opening on the side of the sample holder allowed injection of the illumination beam and an opening on the bottom allowed for emission light collection. An absorber behind the sample holder ensured that no laser light left the miniSPIM platform. The sample container was a square glass cuvette of 1 mm inner diameter, a wall thickness of 0.2 mm, and a length of 50 mm (see Figure 1F). Capillary action facilitated loading liquid samples into the cuvette and, after sample uptake, both ends were either sealed temporarily with wax or permanently with epoxy.

For alignment of the miniSPIM and characterization of the spatial resolution and optical sectioning capability, a sample cuvette was filled with a solution of 1 μm polystyrene beads. A large field view of the light sheet (illumination wavelength 635 nm) propagating through the light scattering bead solution is shown in Figure 2A. The known inner diameter (1 mm) of the sample cuvette served as a reference to obtain the pixel size at the sample. Beam divergence led to a loss of optical sectioning at distances from the image center larger than ~150 μm, which was in good agreement with the calculated Rayleigh length. Hence, in areas of increased light-sheet thickness, more and more beads were illuminated and thus detected despite the distribution of beads in the solution being homogeneous. In the image, this effect can be observed as a higher perceived bead density outside a central region of ~300 μm width (see arrow in Figure 2A). The light-sheet thickness was chosen as a reasonable compromise between axial resolution and the distance over which this sectioning capability could be maintained. Notably, while a light-sheet thinner than the imaging depth of the objective lens (here ~5 μm imaging depth given a relay lens NA of 0.5) can improve the effective axial resolution, the main advantage of using a light

https://doi.org/10.1021/acssensors.1c00607
ACS Sens. 2021, 6, 2654–2663

sheet over epi-illumination is to avoid generating out-of-focus background. An epi-illuminated widefield setup does not provide optical sectioning independent of the depth of focus of the objective lens.

In addition to light-sheet divergence, spherical aberration distorted the image at the field of view periphery, which was expected due to the simplicity of the detection optics compared to fully corrected high-end microscopy objective lenses. For our experiments, limiting the field of view to an undistorted area of ~500 × 500 μm was generally sufficient. Within this spherical aberration-free area, the lateral resolution of the miniSPIM was characterized (see Figure 2B,C). Sufficient optical resolution provided; the image resolution generally corresponds to 2.5−3 times the image pixel size according to the Nyquist−Shannon sampling theorem[30] with Kell factors 0.67−0.8. With a pixel size at the sample of 1.3 μm, the measured lateral resolution of 3.1 μm (Gaussian FWHM, see Figure 2C) is in good alignment with the theory. It also suggests that the numerical aperture (NA) of the system would allow for higher spatial resolutions, if the magnification were to be increased, for example, using a relay lens of shorter focal length. Yet, for the applications presented in the following, this resolution was sufficient and allowed for a relatively high working distance (2 mm) to easily accommodate the sample cuvette (OD 1.4 mm) and holder.

Measuring the Motility of Fluorescent Particles in Solution. Particle tracking as well as fluctuation spectroscopy methods have accurately measured the motion (and size) of particles much smaller (a few nanometers) than the diffraction limit of high-end optics (~200 nm, NA 1.4).[11,31−34] To evaluate the capability of the miniSPIM to quantify the movement of submicron-sized particles, the sample cuvette was filled with dilutions of yellow-green fluorescent particles of 100, 200, and 500 nm diameter, the capillary ends were sealed off with wax, and the samples were subjected to miniSPIM imaging. For the illumination of microparticles, light from a 445 nm laser diode was used, and the green fluorescence was collected through a Kodak Wratten No 55 band pass filter via the mobile device camera. Single particles could be clearly identified in the resulting images (see Figure 3A−C). Videos of 1920 × 1080 pixels were recorded at 29.9 frames per second (fps) with a pixel size at the sample of 935 nm using digital zoom. While digital zoom did not improve the optical resolution, it allowed a live magnified view of the sample on the small screen of the mobile device to help position the specimen and to monitor the sample during the measurement. Since the particles were suspended in a solution, they moved depending on temperature, particle size, and solution viscosity according to the diffusion law. To measure diffusion coefficients, image mean square displacement analysis (iMSD)[11,35] was applied to the image time series recorded. For each sample, a total of 512 frames in a region of 512 ×512 pixels were analyzed; the resulting data are shown in Figure 3D−F. The measured diffusion coefficients were 4.8 $\mu m^2\ s^{-1}$ (100 nm beads), 2.9 $\mu m^2\ s^{-1}$ (200 nm beads), and 0.63 $\mu m^2\ s^{-1}$ (500 nm beads). As expected, an increase in particle diameter resulted in a decrease of the measured diffusion coefficient inversely proportional to the particle size. Notably, for 100 nm beads in an aqueous solution at room temperature, the result is very close to the previously reported diffusion coefficient of 4.4 $\mu m^2\ s^{-1}$ obtained by means of dual-focus fluorescence correlation spectroscopy.[36,37] As the only required input parameters for iMSD analysis are the frame rate and the sample pixel size, no reference measurement with a sample of known diffusion kinetics was needed to yield highly accurate results.

Detection of Microorganisms and Their Motion Type and Rate. Rapid acquisition of a time series of images and analysis with fluorescence correlation spectroscopy in the form of iMSD can also be used to determine the presence and the type and rate of motion of microorganisms. For example, the presence of bacteria in a solution can be easily distinguished from other contaminants by specific fluorescence labeling. In addition, active movement, as exhibited by many bacteria types, should manifest itself in a parabolic shape of the iMSD as a function of lag time instead of the linear relation characteristic of free diffusion, a useful criterion to discern between live and dead bacteria.

To investigate, a solution was prepared containing live bacteria (*Bacillus subtilis*) and membrane stain FM 4-64 which labels both, live and dead bacteria. A single exemplary image of the time series acquired is shown in Figure 4A; the corresponding iMSD analysis is shown in Figure 4B. It can be seen that the bacteria exhibited active motion (quadratic dependence of the MSD) with a measured velocity of 6.0 $\mu m^2\ s^{-1}$. As a reference, for *B. subtilis*, a median swimming speed of 10 $\mu m^2\ s^{-1}$ has been previously reported based on particle tracking.[38] After the measurement, the same sample was subjected to heat shock treatment at 65 °C for 1 min, followed by the repetition of the acquisition. An exemplary image of the acquired image time series is shown in Figure 4C, the corresponding iMSD analysis is shown in Figure 4D. After heat shock treatment, the bacteria no longer displayed active motion but passive diffusion instead (linear dependence of the MSD), similar to the beads shown in Figure 3.

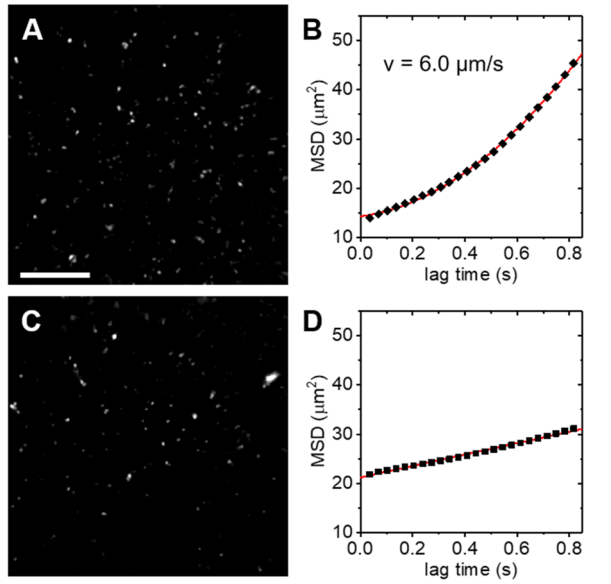

Figure 4. Images and diffusion kinetics of live and dead bacteria. (A) Live *B. subtilis* suspended in buffer solution labeled with membrane stain FM 4-64. Scale bar: 100 μm. (B) Mean square displacement (MSD) as a function of lag time obtained by image correlation analysis of 512 frames each, recorded at 29.9 fps. A quadratic dependence of the MSD characteristic for the active motion was found; the data was fitted with a parabola to quantify the average velocity (6.0 $\mu m\ s^{-1}$). (C) Same *B. subtilis* sample as shown in panel (A), but after heat shock treatment at 65 °C for 1 min. (D) Resulting MSD showed a linear lag time dependence indicative of free diffusion without active motion.

Solvent Polarity Characterization with the Fluorescent Lipid Probe Nile Red. The polarity of lipids, lipid

https://doi.org/10.1021/acssensors.1c00607
ACS Sens. 2021, 6, 2654−2663

membranes, and solvents is an important parameter that can yield insights into the state and processes of many biological and biochemical systems. Nile red (NR) or 9-diethylamino-5H-benzo[α]phenoxazine-5-one is a lipophilic fluorescent probe that has been successfully applied to stain lipid droplets,[39] to measure total lipid content,[40] and to characterize the organization of membranes.[41,42] The fluorescence emission of NR, an uncharged red phenoxazone dye, spectrally shifts depending on immediate environmental properties that can change the dipole moment upon excitation.[43,44] To characterize the spectral shift, the general polarization (GP) method is an established ratiometric assay based on measuring the intensity in two different spectral windows at shorter and longer wavelengths within the emission spectrum of the probe.[45] The sensor of most mobile device cameras is covered with a Bayer filter that overlays an RGBG (red-green-blue-green) pattern over the sensor pixels in a 2 × 2 layout to record color images. Typically, the maximum transmissions of such Bayer filters are in the range of 500−580 nm for the green pixels, and 580−650 nm for the red pixels, which is ideal to detect NR peak emission shifts from ~530 nm (in heptane) to ~650 nm (in water).[39] To investigate, three different NR solutions were prepared in solvents of decreasing polarity. NR fluorescence was excited with 445 nm light and scattered light was eliminated with a Kodak Wratten No 12 long-pass filter. Example images of NR in dimethyl sulfoxide (DMSO), glycerol, and in olive oil are shown in Figure 5A−C. After extracting the green and red channels from the RGB images, the GP was quantified in Figure 5D that decreased with decreasing solution polarity as expected. Several images at different illumination intensities were acquired to show that the GP was measured consistently and independently of the excitation power. These results indicate that the miniSPIM, coupled to a color camera, is well suited for ratiometric measurements of spectral shifts that can be very useful for a wide variety of biochemical assays. Notably, despite the change in refractive index of the NR samples (DMSO: n = 1.48, glycerol: n = 1.47, olive oil: n = 1.44−1.47) compared to aqueous solutions (n = 1.33), no realignment of the miniSPIM was needed. Robust operation is important for field applications where realignment could be difficult.

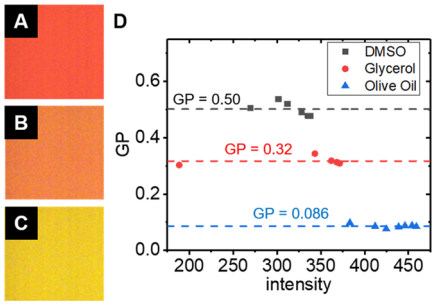

Figure 5. General polarization (GP) measurements of Nile Red (NR) solutions. Example miniSPIM color images of NR in (A) DMSO, (B) glycerol, and (C) olive oil. (D) GPs of the three NR solutions (average values printed in the graph) decreased with decreasing solvent polarity independently of the excitation intensity.

Autofluorescence Imaging of a Live Zebrafish Embryo. A popular model in developmental biology is the zebrafish, which can be used, for example, to study the effects of chemicals such as the toxicity of drug candidates[46] as well as environmental effects of chemicals used in agriculture including pesticides and herbicides.[47] As the miniSPIM is inexpensive, robust, portable, and battery powered, it is ideally suited for field research. Applications include the characterization of the development of embryos and larvae of small animals that live in close proximity to areas where agricultural chemicals are used. To illustrate such application, 72 h post fertilization (hpf), zebrafish embryos were anesthetized with tricaine methanesulfonate. After uptake into a 1 mm inner diameter cuvette, transmission as well as autofluorescence color images (445 nm excitation) were taken with the miniSPIM; examples are shown in Figure 6A−E. Clear differences in the emission spectrum were observed in different organs, for example, the eye yielded strong fluorescence in both the blue and green channels but not in the red channel. As an alternative to measuring intrinsic fluorescence, specific components of the organism could be highlighted by incubation with fluorescence stains before imaging. By manually sliding the sample cuvette through the sample holder channel of the miniSPIM in a stepwise manner, several images of the same sample were acquired and stitched together in Figure 6F.

One of the key advantages of light-sheet microscopy is the capability to rapidly acquire optically sectioned 3D data. The acquisition of image stacks can be achieved by either translating the sample with a motorized stage or by synchronized movement of the light sheet and detection lens focus. Both approaches typically require expensive and bulky positioning systems that can provide high accuracy. Instead, here the sample was passively moved through the light sheet and detection lens focus with independently running video acquisition to collect a stack of z sections. With the miniSPIM in a horizontal position (mobile device screen facing upwards), the zebrafish suspended inside the sample cuvette in glycerol was slowly sinking down to the backside of the cuvette. During this movement, the equilibrium between gravitational pull and fluid friction due to laminar flow produced a constant sample translation speed. The RGB-merged maximum intensity projections of 3D data of a zebrafish head and trunk section acquired in this fashion are shown in Figure 7 and Supporting Information, Video S1. The symmetry of the eye was exploited to determine the spacing of the z sections from the known xy dimensions. Alternatively, reference objects of known size (e.g., 15 μm diameter beads) could be added to the sample to determine the z-section spacing.

In addition to providing the ability to measure the motion of particles, fast time-lapse imaging of a single z-section can also enable the characterization of highly dynamic processes in living specimen. As an example, Figure 8A−D shows different time points of a beating heart of a 72 hpf zebrafish embryo acquired at 30 fps. The regions marked with arrows indicate blood entering (I_1) and leaving (I_2) the beating heart in comparison to a region without pulsatile blood flow (I_3). The corresponding intensity time traces are shown in Figure 8E−G. In Figure 8A, blood was pumped out as the heart contracted while backflow was prevented by valves, resulting in $I_1 < I_2$. In Figure 8B, the heart was relaxed resulting in $I_1 = I_2$. In Figure 8C, blood was pumped into the heart while outflow was prevented by valves, resulting in $I_1 > I_2$. In Figure 8D, the cycle repeated with $I_1 < I_2$. From the time traces, a heart rate of 1.2 Hz corresponding to 72 beats per minute (bpm) was measured. The entire 10 s long sequence can be seen in Supporting Information, Video S2. This relatively slow heartbeat can be attributed to the effects of tricaine anesthesia and measurement at room temperature (20 °C). For unanesthetized zebrafish embryos at 25−32 °C, a heart rate in the range of 120−180 bpm is typical.[48−50] In a recent

https://doi.org/10.1021/acssensors.1c00607
ACS Sens. 2021, 6, 2654−2663

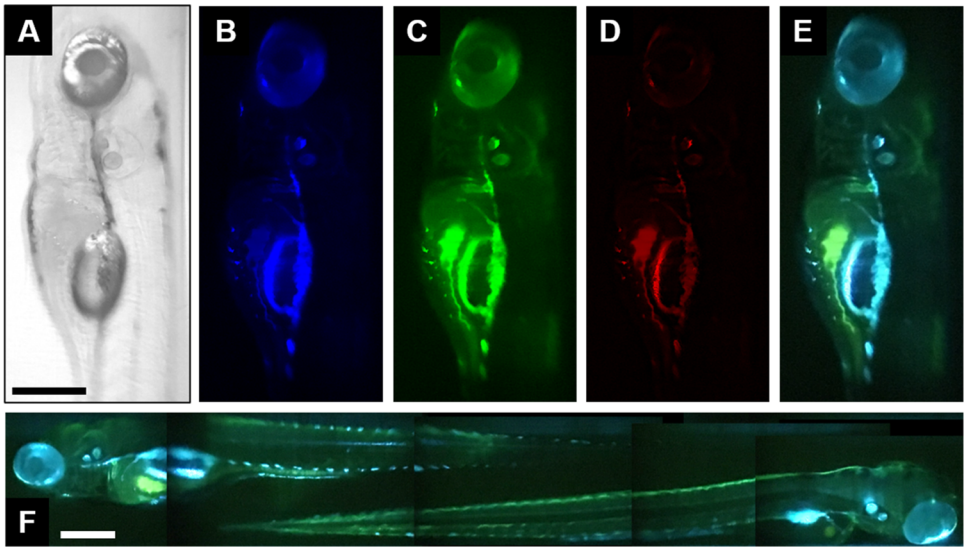

Figure 6. miniSPIM images of 72 hpf zebrafish embryos. (A) Transmission image. (B) Blue, (C) green, and (D) red images of the (E) RGB camera image overlay acquired with 445 nm excitation. (F) By stepwise manual translation of the sample cuvette, several tiles of the same sample were acquired and stitched together in a mosaic image.

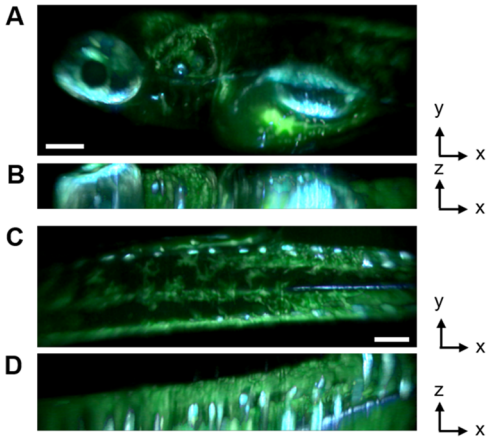

Figure 7. miniSPIM 3D data of a 72 hpf zebrafish embryo. (A) Merged RGB maximum intensity projection of the zebrafish head portion along the *z*-axis. (B) Maximum intensity projection of the zebrafish head portion along the *y*-axis. (C) Maximum intensity projection of the zebrafish trunk portion along the *z*-axis. (D) Maximum intensity projection of the zebrafish trunk portion along the *y*-axis. Scale bars: 100 μm.

study, embryonic zebrafish expressing fluorescent markers in their cardiovascular tissues (Tg-(Kdrl:GFP^{s843}:gata1:DsRED^{sd2})) were imaged with high resolution to track the motion of the heart wall tissue (GFP-labeled) and blood pool variation (DsRED-labeled); the presence of a mild phase shift between the two time series (area and blood pool) was observed with the blood pool content delayed with respect to the area variation of the heart chamber.[49] While the zebrafish were unlabeled in the work presented here, we hypothesize that heart wall tissue can be distinguished from red blood cells via differences in their autofluorescence spectra. In cardiac tissue, when excited by visible light, the signal is dominated by cellular autofluorescence in the wavelength region of 490−560 nm, for which oxidized mitochondrial flavins and flavoproteins are the major contributors.[51] In contrast, hemoglobin (Hb) molecules emit broadband fluorescence over 550−750 nm when excited by visible light[52] (in addition to tryptophan emission when excited at 280 nm[53]). To investigate, five representative peaks of the intensity time series of the whole heart (boxed region in Figure 8A) were plotted for the green (500−580 nm) and the red channel (580−650 nm) in Figure 8H. A slight phase shift (70 ms) was observed with the green channel peaks preceding the red channel peaks, which is in alignment with the chronologies of blood pool and area variation reported by De Luca et al.[49]

DISCUSSION

This work shows a miniaturized version of a light-sheet microscope, the miniSPIM, that is of low cost, robust, and highly portable. Based on widely available and inexpensive parts, potential usages for the miniSPIM include biosensing, education, and field research. Example applications shown here measured the motion of microparticles and micro-organisms, characterized spectral shifts of polarity sensing dyes, and demonstrated multichannel 3D and time-lapse fluorescence imaging of live zebrafish embryos. Of particular interest could be the detection of bacterial/microorganism contamination of water, food sources, and contamination of medical supplies in remote areas, as well as environmental and ecology research, for example, studying the impact of chemicals used in agriculture. Field application was underscored by label-free measurement of the embryonic zebrafish heart rate and phase shift between heart chamber contraction and blood pool content based on two channel autofluorescence imaging. Zebrafish cardiac rate fluctuations are an important readout as they can be induced by factors such as temperature, genetic and chemical-induced alterations.

With a component cost of <$200, the miniSPIM could also be a valuable device for educational purposes to teach the principle of optics and imaging, particle motion in a fluid environment, and to visualize basic developmental biology. The processing power of state-of-the-art smart mobile devices also allows on-site analysis of light-sheet microscopy data. Being based on a smartphone, software ("apps") could be developed to accommodate specific needs including image analysis, cloud-based data storage, and sharing of the results. Alternatively, more demanding algorithms could be executed on a server or cloud

https://doi.org/10.1021/acssensors.1c00607
ACS Sens. 2021, 6, 2654−2663

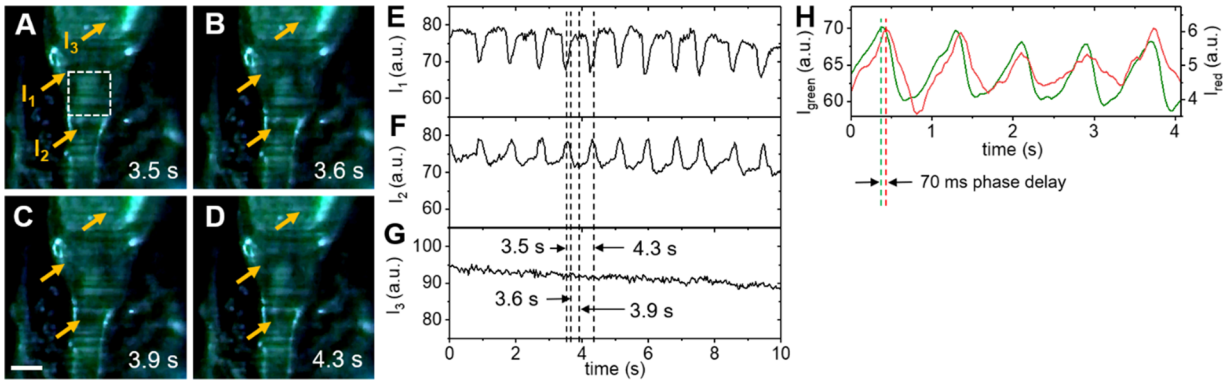

Figure 8. miniSPIM imaging of a beating 72 hpf zebrafish embryo heart. (A–D) Single RGB-merged sections of different time points of a beating zebrafish heart acquired at 30 fps. (E–G) Intensity time traces (RGB averages) quantified in regions I_1–I_3 marked by arrows in panels (A–D). (H) Intensity time traces in the green and red channels averaged in the region outlined by the white box in panel (A). A rolling average of five time points was applied to a 5 peak/4 s snippet of the time series to better visualize the phase shift. A phase delay of 70 ms was measured between peaks with the red channel trailing the green channel. Scale bar: 50 μm.

after data upload, followed by sending back the results to the device. While passive 3D imaging through sedimentation of the sample in a viscous medium (here: glycerol) is an easy solution that does not require extra components, the sample z translation speed cannot be precisely controlled, which may result in motion blur. Also, such translation does not work for samples mounted in a gel or other nonfluid mounting media. More precise z stacking capable of sub-micron-scale motion independent of the sample mounting medium could be achieved by adding a 3D-printed flexure stage actuated by inexpensive miniature stepper motors[54,55] or piezo buzzers[56] to further improve the miniSPIM design.

MATERIALS AND METHODS

Bacteria. *B. subtilis* were grown in LB broth to a concentration of OD_{600} = 0.5, diluted in Minimal Broth, and fluorescently stained with FM 4-64 dye (T13320, ThermoFisher) before imaging. Stained bacteria solution was loaded into 1 mm of ID square capillaries (8100-050, Vitrocom) and the ends were sealed with epoxy. Heat shock treatment was performed by placing the bacteria-containing cuvette onto a heat plate at 65 °C for 1 min.

Zebrafish. Zebrafish lines were maintained and bred at 26.5 °C. Embryos were raised at 28.5 °C and staged in hours post fertilization (hpf). Embryos were treated with 0.003% phenylthiourea (PTU, Sigma-Aldrich) at 8 hpf to delay pigmentation and were anesthetized by 0.04% MS-222 (Sigma-Aldrich) prior to live imaging.

miniSPIM Imaging. Images were captured on a mobile phone equipped with a 12 megapixel camera (1.22 μm camera chip pixel size) in RAW format to avoid JPG compression artifacts. The autofocus function was disabled during imaging. Still images were captured in a format of 4032 × 3024 pixels; exposure time was adjusted to not saturate the 8 bit range of the image sensor. Time series were acquired in a format of 1920 × 1080 pixels at 29.9 fps. Using the digital zoom function, the sample pixel size was adjusted between 0.935 and 1.3 μm. Notably, digital zoom did not change the optical magnification and therefore did not improve the optical resolution of the resulting images. Digital zoom cropped a region of the image and enlarged the cropped part on the screen of the mobile device. In principle, the digital zoom was not required for the experiment. However, digital zoom allowed a magnified view of the sample on the rather small screen of the mobile device to help position the specimen and to facilitate monitor the light-sheet position and sample during the measurement. The pixel size was calculated using the inner diameter (1 mm) of the sample cuvette/capillary as a reference. Images and videos were visualized in Fiji ImageJ 1.52p. Data was graphed with OriginPro 2017 (OriginLab).

miniSPIM Alignment. The cylinder lens, laser beam aperture, and laser were mounted to the base plate with screws with rubber O-rings placed between the mount and a secondary mount. The secondary mount was attached to the base plate in the same manner, but with perpendicular screw axes. Hence, by tightening or loosening the respective screws, compression or extension of the rubber O-ring allowed for a ~0.8 mm translation along the screw axis. For alignment, the cylinder lens and aperture were removed. Using the screws on the laser holder, the beam was moved until it illuminated the sample cuvette at the center. After this coarse alignment, the aperture was installed and adjusted to crop the central portion of the beam. Then, the cylinder lens was installed and a solution of 1 μm of polystyrene microbeads was prepared. Without the emission filter, light scattered off the particles was imaged. First, the two screws moving the cylinder lens closer or further away from the base plate were adjusted to overlay the light sheet with the focal plane of the detection lens. At the correct position, the beads will appear sharp in the image. The light-sheet tip was corrected by tightening/loosening only one side. In a second step, the screws moving the cylinder lens along the illumination axis were adjusted to move the light sheet focus into the center of the field of view. Beam divergence will inevitably lead to reduced optical sectioning at the field of view periphery. Light-sheet tilt was corrected by tightening/loosening only one side.

GP Analysis. Matlab (R2019a, Mathworks) was used to analyze GP data. First, RGB image data was separated into green (I_g) and red channels (I_r). Then, for each image pixel, the GP was calculated according to

$$\mathrm{GP} = \frac{I_g - I_r}{I_g + I_r} \tag{1}$$

and all pixels were averaged to yield a final GP value for each image.

iMSD Analysis. Particle dynamics were analyzed in Matlab (R2019a, Mathworks) with the image mean square displacement method as previously described.[11] An immobile fraction was substracted before the spatiotemporal correlation of the image data. To quantify free diffusion, the spatiotemporal correlation G_D (ξ,ψ,τ) was modeled with a Gaussian,

$$G_D(\xi, \psi, \tau) = g_D(\tau)\exp\left(-\frac{\xi^2 + \psi^2}{\sigma_r^2(\tau)}\right) \tag{2}$$

with pixel lags ξ and ψ and time lag τ. The width σ_r (τ) represents the mean square displacement of the particles within the image

$$\sigma_r^2(\tau) = 4D\tau + \sigma_0^2 \tag{3}$$

with the diffusion coefficient, D, resulting from the slope. σ_0^2 represents the convolution of the average particle size and the point spread function waist. For 3D diffusion, the amplitude, g_D (τ), is determined by

https://doi.org/10.1021/acssensors.1c00607
ACS Sens. 2021, 6, 2654–2663

$$g_D(\tau) = \frac{\gamma}{N}(\pi\sigma_r^2(\tau))^{-3/2} \quad (4)$$

where N is the average number of particles inside the observation volume and $\gamma = 0.35$ is a correction factor for the shape of the volume. For active transport, the additional broadening of the correlation peak was accounted for by a velocity term, $v^2\tau^2$, yielding

$$\sigma_r^2(\tau) = v^2\tau^2 + 4D\tau + \sigma_0^2 \quad (5)$$

to recover the average speed of the particles.

Spatial Resolution Characterization. For a given numerical aperture, NA, and light wavelength, λ, the Gaussian beam waist can be paraxially approximated as

$$w_r = \frac{2\lambda}{\pi NA} \quad (6)$$

The Rayleigh length is the distance along the propagation direction of a beam from the waist to where the beam radius has increased by a factor $\sqrt{2}$

$$z_R = \frac{\pi w_r^2}{\lambda} \quad (7)$$

Experimentally, the lateral resolution was obtained by fitting the intensity profile of single beads with a Gaussian distribution,

$$I(x) = I_0 + \frac{A\cdot\exp\left(\frac{-4\ln(2)(x-x_c)^2}{w^2}\right)}{w\sqrt{\frac{\pi}{4\ln(2)}}} \quad (8)$$

with w the full width at half-maximum (FWHM), I_0 the offset, A the peak amplitude, and x_c the peak center position.

Ethical Approval. All zebrafish work was performed in accordance with NIH guidelines and was approved by the Institutional Animal Care and Use Committee (IACUC) of the University of California, Irvine. All experiments were carried out in accordance with relevant guidelines and regulations.

■ ASSOCIATED CONTENT

Supporting Information

The Supporting Information is available free of charge at https://pubs.acs.org/doi/10.1021/acssensors.1c00607.

360° RGB-merged maximum intensity projections of 3D data of a zebrafish head section with two perpendicular projections shown in Figure 7A,B (Movie S1) (AVI)

Ten seconds long time sequence of a beating heart of a 72 hpf zebrafish embryo obtained at 30 fps with select time points shown in Figure 8A−D (Movie S2) (AVI)

■ AUTHOR INFORMATION

Corresponding Author

Per Niklas Hedde − *Beckman Laser Institute, University of California Irvine, Irvine, California 92612, United States; Department of Pharmaceutical Sciences and Laboratory for Fluorescence Dynamics, University of California Irvine, Irvine, California 92697, United States;* orcid.org/0000-0002-2994-369X; Email: phedde@uci.edu

Complete contact information is available at: https://pubs.acs.org/10.1021/acssensors.1c00607

Author Contributions

P.N.H. designed and built the miniSPIM, prepared samples, acquired, and analyzed the data. P.N.H. wrote the manuscript and conceived the project.

Notes

The author declares the following competing financial interest(s): PNH has filed a patent under US Provisional Patent Application No. 62/993,610.

Upon a reasonable request, the data will be made available to other researchers.

■ ACKNOWLEDGMENTS

P.N.H. is supported by the National Institute of General Medical Sciences of the National Institutes of Health (R21GM135493). The experiments reported in this publication were performed at the Laboratory for Fluorescence Dynamics (LFD) at the University of California, Irvine (UCI). The LFD is supported jointly by the National Institute of General Medical Sciences of the National Institutes of Health (P41GM103540) and UCI. Special thanks go to Leonel Malacrida and Andrés Kamaid from the Institute Pasteur of Montevideo, Uruguay for assisting with the Nile Red experiments and for support with the preparation of the zebrafish embryos. Many thanks also go to Irene Vorontsova from the lab of Thomas F. Schilling at UC Irvine for providing zebrafish embryos and to Michael Morris from the lab of James S. Nowick at UC Irvine for providing bacteria samples.

■ REFERENCES

(1) Siedentopf, H.; Zsigmondy, R. Uber Sichtbarmachung Und Größenbestimmung Ultramikoskopischer Teilchen, Mit Besonderer Anwendung Auf Goldrubingläser. *Ann. Phys.* **1902**, *315*, 1−39.

(2) Huisken, J.; Swoger, J.; Del Bene, F.; Wittbrodt, J.; Stelzer, E. H. K. Optical Sectioning Deep inside Live Embryos by Selective Plane Illumination Microscopy. *Science* **2004**, *305*, 1007−1009.

(3) Voie, A. H.; Burns, D. H.; Spelman, F. A. Orthogonal-plane Fluorescence Optical Sectioning: Three-dimensional Imaging of Macroscopic Biological Specimens. *J. Microsc.* **1993**, *170*, 229−236.

(4) Santi, P. A. Light Sheet Fluorescence Microscopy: A Review. *J. Histochem. Cytochem.* **2011**, *59*, 129−138.

(5) Lemon, W. C.; Pulver, S. R.; Höckendorf, B.; McDole, K.; Branson, K.; Freeman, J.; Keller, P. J. Whole-Central Nervous System Functional Imaging in Larval Drosophila. *Nat. Commun.* **2015**, *6*, No. 7924.

(6) Wu, Y.; Ghitani, A.; Christensen, R.; Santella, A.; Du, Z.; Rondeau, G.; Bao, Z.; Colón-Ramos, D.; Shroff, H. Inverted Selective Plane Illumination Microscopy (ISPIM) Enables Coupled Cell Identity Lineaging and Neurodevelopmental Imaging in Caenorhabditis Elegans. *Proc. Natl. Acad. Sci. U.S.A.* **2011**, *108*, 17708−17713.

(7) Stefaniuk, M.; Gualda, E. J.; Pawlowska, M.; Legutko, D.; Matryba, P.; Koza, P.; Konopka, W.; Owczarek, D.; Wawrzyniak, M.; Loza-Alvarez, P.; et al. Light-Sheet Microscopy Imaging of a Whole Cleared Rat Brain with Thy1-GFP Transgene. *Sci. Rep.* **2016**, *6*, No. 28209.

(8) Glaser, A. K.; Reder, N. P.; Chen, Y.; McCarty, E. F.; Yin, C.; Wei, L.; Wang, Y.; True, L. D.; Liu, J. T. C. Light-Sheet Microscopy for Slide-Free Non-Destructive Pathology of Large Clinical Specimens. *Nat. Biomed. Eng.* **2017**, *1*, No. 0084.

(9) Maioli, V.; Chennell, G.; Sparks, H.; Lana, T.; Kumar, S.; Carling, D.; Sardini, A.; Dunsby, C. Time-Lapse 3-D Measurements of a Glucose Biosensor in Multicellular Spheroids by Light Sheet Fluorescence Microscopy in Commercial 96-Well Plates. *Sci. Rep.* **2016**, *6*, No. 37777.

(10) Theer, P.; Dragneva, D.; Knop, M. ΠsPIM: High NA High Resolution Isotropic Light-Sheet Imaging in Cell Culture Dishes. *Sci. Rep.* **2016**, *6*, No. 32880.

(11) Hedde, P. N.; Stakic, M.; Gratton, E. Rapid Measurement of Molecular Transport and Interaction inside Living Cells Using Single Plane Illumination. *Sci. Rep.* **2014**, *4*, No. 7048.

(12) Hedde, P. N.; Malacrida, L.; Ahrar, S.; Siryaporn, A.; Gratton, E. SideSPIM − Selective Plane Illumination Based on a Conventional Inverted Microscope. *Biomed. Opt. Express* **2017**, *8*, 3918−3937.

(13) Gualda, E. J.; Vale, T.; Almada, P.; Feijó, J. A.; Martins, G. G.; Moreno, N. OpenSpinMicroscopy: An Open-Source Integrated Microscopy Platform. *Nat. Methods* **2013**, *10*, 599−600.
(14) Diederich, B.; Lachmann, R.; Carlstedt, S.; Marsikova, B.; Wang, H.; Uwurukundo, X.; Mosig, A. S.; Heintzmann, R. A Versatile and Customizable Low-Cost 3D-Printed Open Standard for Microscopic Imaging. *Nat. Commun.* **2020**, *11*, No. 5979.
(15) Pitrone, P. G.; Schindelin, J.; Stuyvenberg, L.; Preibisch, S.; Weber, M.; Eliceiri, K. W.; Huisken, J.; Tomancak, P. OpenSPIM: An Open-Access Light-Sheet Microscopy Platform. *Nat. Methods* **2013**, *10*, 598−599.
(16) Gualda, E. J.; Pereira, H.; Vale, T.; Estrada, M. F.; Brito, C.; Moreno, N. SPIM-Fluid: Open Source Light-Sheet Based Platform for High-Throughput Imaging. *Biomed. Opt. Express* **2015**, *6*, 4447−4456.
(17) Guan, Z.; Lee, J.; Jiang, H.; Dong, S.; Jen, N.; Hsiai, T.; Ho, C.-M.; Fei, P. Compact Plane Illumination Plugin Device to Enable Light Sheet Fluorescence Imaging of Multi-Cellular Organisms on an Inverted Wide-Field Microscope. *Biomed. Opt. Express* **2016**, *7*, 194−208.
(18) Bruns, T.; Schickinger, S.; Schneckenburger, H. Single Plane Illumination Module and Micro-Capillary Approach for a Wide-Field Microscope. *J. Vis. Exp.* **2014**, *90*, No. 51993.
(19) Jiang, H.; Zhu, T.; Zhang, H.; Nie, J.; Guan, Z.; Ho, C. M.; Liu, S.; Fei, P. Droplet-Based Light-Sheet Fluorescence Microscopy for High-Throughput Sample Preparation, 3-D Imaging and Quantitative Analysis on a Chip. *Lab Chip* **2017**, *17*, 2193−2197.
(20) Wu, J.; Li, J.; Chan, R. K. Y. A Light Sheet Based High Throughput 3D-Imaging Flow Cytometer for Phytoplankton Analysis. *Opt. Express* **2013**, *21*, 14474−14480.
(21) Voigt, F. F.; Kirschenbaum, D.; Platonova, E.; Pagès, S.; Campbell, R. A. A.; Kastli, R.; Schaettin, M.; Egolf, L.; van der Bourg, A.; Bethge, P.; et al. The MesoSPIM Initiative: Open-Source Light-Sheet Microscopes for Imaging Cleared Tissue. *Nat. Methods* **2019**, *16*, 1105−1108.
(22) Breslauer, D. N.; Maamari, R. N.; Switz, N. A.; Lam, W. A.; Fletcher, D. A. Mobile Phone Based Clinical Microscopy for Global Health Applications. *PLoS One* **2009**, *4*, No. e6320.
(23) Collins, J. T.; Knapper, J.; Stirling, J.; Mduda, J.; Mkindi, C.; Mayagaya, V.; Mwakajinga, G. A.; Nyakyi, P. T.; Sanga, V. L.; Carbery, D.; et al. Robotic Microscopy for Everyone: The OpenFlexure Microscope. *Biomed. Opt. Express* **2020**, *11*, 2447−2460.
(24) Zhu, W.; Pirovano, G.; O'Neal, P. K.; Gong, C.; Kulkarni, N.; Nguyen, C. D.; Brand, C.; Reiner, T.; Kang, D. Smartphone Epifluorescence Microscopy for Cellular Imaging of Fresh Tissue in Low-Resource Settings. *Biomed. Opt. Express* **2020**, *11*, 89−98.
(25) Wei, Q.; Qi, H.; Luo, W.; Tseng, D.; Ki, S. J.; Wan, Z.; Göröcs, Z.; Bentolila, L. A.; Wu, T. T.; Sun, R.; et al. Fluorescent Imaging of Single Nanoparticles and Viruses on a Smart Phone. *ACS Nano* **2013**, *7*, 9147−9155.
(26) Yelleswarapu, V. R.; Jeong, H. H.; Yadavali, S.; Issadore, D. Ultra-High Throughput Detection (1 Million Droplets per Second) of Fluorescent Droplets Using a Cell Phone Camera and Time Domain Encoded Optofluidics. *Lab Chip* **2017**, *17*, 1083−1094.
(27) Wu, T. F.; Yen, T. M.; Han, Y.; Chiu, Y. J.; Lin, E. Y. S.; Lo, Y. H. A Light-Sheet Microscope Compatible with Mobile Devices for Label-Free Intracellular Imaging and Biosensing. *Lab Chip* **2014**, *14*, 3341−3348.
(28) Sung, Y.; Campa, F.; Shih, W.-C. Open-Source Do-It-Yourself Multi-Color Fluorescence Smartphone Microscopy. *Biomed. Opt. Express* **2017**, *8*, 5075−5086.
(29) Zhu, H.; Yaglidere, O.; Su, T. W.; Tseng, D.; Ozcan, A. In *Wide-Field Fluorescent Microscopy on a Cell-Phone*, 2011 Annual International Conference of the IEEE Engineering in Medicine and Biology Society; IEEE, 2011; pp 6801−6804.
(30) Shannon, C. E. Communication in the Presence of Noise. *Proc. IRE* **1949**, *37*, 10−21.
(31) Magde, D.; Elson, E.; Webb, W. W. Thermodynamic Fluctuations in a Reacting System Measurement by Fluorescence Correlation Spectroscopy. *Phys. Rev. Lett.* **1972**, *29*, 705−708.
(32) Magde, D.; Elson, E. L.; Webb, W. W. Fluorescence Correlation Spectroscopy. II. An Experimental Realization. *Biopolymers* **1974**, *13*, 29−61.
(33) Röcker, C.; Pötzl, M.; Zhang, F.; Parak, W. J.; Nienhaus, G. U. A Quantitative Fluorescence Study of Protein Monolayer Formation on Colloidal Nanoparticles. *Nat. Nanotechnol.* **2009**, *4*, 577−580.
(34) Yildiz, A.; Tomishige, M.; Vale, R. D.; Selvin, P. R. Kinesin Walks Hand-Over-Hand. *Science* **2004**, *303*, 676−678.
(35) Di Rienzo, C.; Gratton, E.; Beltram, F.; Cardarelli, F. Fast Spatiotemporal Correlation Spectroscopy to Determine Protein Lateral Diffusion Laws in Live Cell Membranes. *Proc. Natl. Acad. Sci. U.S.A.* **2013**, *110*, 12307−12312.
(36) Müller, C. B.; Weiß, K.; Richtering, W.; Loman, A.; Enderlein, J. Calibrating Differential Interference Contrast Microscopy with Dual-Focus Fluorescence Correlation Spectroscopy. *Opt. Express* **2008**, *16*, 4322−4329.
(37) Kapusta, P. Absolute Diffusion Coefficients: Compilation of Reference Data for FCS Calibration, 2010. https://www.picoquant.com/images/uploads/page/files/7353/appnote_diffusioncoefficients.pdf.
(38) Bedrossian, M.; El-Kholy, M.; Neamati, D.; Nadeau, J. A Machine Learning Algorithm for Identifying and Tracking Bacteria in Three Dimensions Using Digital Holographic Microscopy. *AIMS Biophys.* **2018**, *5*, 36−49.
(39) Greenspan, P.; Fowler, S. D. Spectrofluorometric Studies of the Lipid Probe, Nile Red. *J. Lipid Res.* **1985**, *26*, 781−789.
(40) Kou, Z.; Bei, S.; Sun, J.; Pan, J. Fluorescent Measurement of Lipid Content in the Model Organism Chlamydomonas Reinhardtii. *J. Appl. Phycol.* **2013**, *25*, 1633−1641.
(41) Kucherak, O. A.; Oncul, S.; Darwich, Z.; Yushchenko, D. A.; Arntz, Y.; Didier, P.; Mély, Y.; Klymchenko, A. S. Switchable Nile Red-Based Probe for Cholesterol and Lipid Order at the Outer Leaflet of Biomembranes. *J. Am. Chem. Soc.* **2010**, *132*, 4907−4916.
(42) Sameni, S.; Malacrida, L.; Tan, Z.; Digman, M. A. Alteration in Fluidity of Cell Plasma Membrane in Huntington Disease Revealed by Spectral Phasor Analysis. *Sci. Rep.* **2018**, *8*, No. 734.
(43) Mukherjee, S.; Raghuraman, H.; Chattopadhyay, A. Membrane Localization and Dynamics of Nile Red: Effect of Cholesterol. *Biochim. Biophys. Acta, Biomembr.* **2007**, *1768*, 59−66.
(44) Golini, C. M.; Williams, B. W.; Foresman, J. B. Further Solvatochromic, Thermochromic, and Theoretical Studies on Nile Red. *J. Fluoresc.* **1998**, *8*, 395−404.
(45) Parasassi, T.; De Stasio, G.; d'Ubaldo, A.; Gratton, E. Phase Fluctuation in Phospholipid Membranes Revealed by Laurdan Fluorescence. *Biophys. J.* **1990**, *57*, 1179−1186.
(46) Cassar, S.; Adatto, I.; Freeman, J. L.; Gamse, J. T.; Iturria, I.; Lawrence, C.; Muriana, A.; Peterson, R. T.; Van Cruchten, S.; Zon, L. I. Use of Zebrafish in Drug Discovery Toxicology. *Chem. Res. Toxicol.* **2020**, *33*, 95−118.
(47) Schweizer, M.; Brilisauer, K.; Triebskorn, R.; Forchhammer, K.; Köhler, H. R. How Glyphosate and Its Associated Acidity Affect Early Development in Zebrafish (Danio Rerio). *PeerJ* **2019**, *7*, No. e7094.
(48) Baker, K.; Warren, K. S.; Yellen, G.; Fishman, M. C. Defective "Pacemaker" Current (Ih) in a Zebrafish Mutant with a Slow Heart Rate. *Proc. Natl. Acad. Sci. U.S.A.* **1997**, *94*, 4554−4559.
(49) De Luca, E.; Zaccaria, G. M.; Hadhoud, M.; Rizzo, G.; Ponzini, R.; Morbiducci, U.; Santoro, M. M. ZebraBeat: A Flexible Platform for the Analysis of the Cardiac Rate in Zebrafish Embryos. *Sci. Rep.* **2014**, *4*, No. 4898.
(50) Gierten, J.; Pylatiuk, C.; Hammouda, O. T.; Schock, C.; Stegmaier, J.; Wittbrodt, J.; Gehrig, J.; Loosli, F. Automated High-Throughput Heartbeat Quantification in Medaka and Zebrafish Embryos under Physiological Conditions. *Sci. Rep.* **2020**, *10*, No. 2046.
(51) Chorvat, D.; Kirchnerova, J.; Cagalinec, M.; Smolka, J.; Mateasik, A.; Chorvatova, A. Spectral Unmixing of Flavin Autofluorescence Components in Cardiac Myocytes. *Biophys. J.* **2005**, *89*, L55−L57.
(52) Hui, Y. Y.; Su, L. J.; Chen, O. Y.; Chen, Y. T.; Liu, T. M.; Chang, H. C. Wide-Field Imaging and Flow Cytometric Analysis of Cancer

Cells in Blood by Fluorescent Nanodiamond Labeling and Time Gating. *Sci. Rep.* **2014**, *4*, No. 5574.
(53) Alpert, B.; Jameson, D. M.; Weber, G. Tryptophan emission from human hemoglobin and its isolated subunits. *Photochem. Photobiol.* **1980**, *31*, 1−4.
(54) Collins, J. T.; Knapper, J.; Stirling, J.; Mduda, J.; Mkindi, C.; Mayagaya, V.; Mwakajinga, G. A.; Nyakyi, P. T.; Sanga, V. L.; Carbery, D.; et al. Robotic Microscopy for Everyone: The OpenFlexure Microscope. *Biomed. Opt. Express* **2020**, *11*, 2447−2460.
(55) Sharkey, J. P.; Foo, D. C. W.; Kabla, A.; Baumberg, J. J.; Bowman, R. W. A One-Piece 3D Printed Flexure Translation Stage for Open-Source Microscopy. *Rev. Sci. Instrum.* **2016**, *87*, No. 025104.
(56) Lee, S. H. Note: A 3D-Printed Flexure Nanostage Driven by Piezo Buzzers. *Rev. Sci. Instrum.* **2018**, *89*, No. 106106.

https://doi.org/10.1021/acssensors.1c00607
ACS Sens. 2021, 6, 2654−2663